Porosity and Transport Property Relationships in Fractured Yates Amphibolite

Meryn Martinchick

GEOL 394: Senior Thesis

Submitted in partial fulfillment
of the Geology Major and B.S. Degree,
University of Maryland, College Park

Advisor: Dr. Wenlu Zhu

Mentors: Dr. Tommaso Mandolini and Dr. Travis Hager

April 28th, 2026

Abstract

Enhanced Geothermal Systems (EGS) involve engineering artificial fractures within hot, impermeable rock deep beneath the Earth's surface. Cold water is injected into the engineered fracture network, where it circulates through the hot rock and absorbs thermal energy. The heated water is then pumped back to the surface, where it rapidly flashes into steam and drives a turbine to produce electricity. This closed-loop process provides a reliable, low-carbon energy source with the potential for widespread deployment, greatly diminishing the geographical limitations traditionally associated with geothermal energy and enabling electricity generation in regions that lack naturally occurring hydrothermal resources.

The primary challenge in developing effective EGS reservoirs lies in creating and sustaining a well-connected fracture network to enable efficient heat transfer from the hot rock to the circulating fluid. At the same time, the reservoir must remain mechanically and hydraulically stable, resisting issues such as fracture closure, induced seismicity, or fluid loss to surrounding formations. Overcoming these complexities is critical to maximizing heat extraction efficiency and ensuring the long-term viability of EGS as a dependable, renewable energy resource. Funded by the Department of Energy, the Sanford Underground Research Facility (SURF) in Lead, South Dakota, provides a unique controlled environment for studying subsurface processes, enabling direct access to crystalline rock under relevant pressures, temperatures, and stress conditions for EGS. The SURF testbed allows researchers to conduct in situ experiments on fracture generation while monitoring fluid chemistry, electrical resistivity, temperature, and seismic responses. The principal goal is to develop the ability to predict and control flow through fracture networks for EGS.

In this study, fracture complexity and porosity were investigated in relation to the permeability and conductivity in rocks from the SURF testbed. I focus on four amphibolite samples, DML1, DML5, TS4, and TS41004, collected from the SURF testing wells. These samples were mechanically fractured at room temperature under confining pressures ranging from 35-150 MPa, and pore fluid pressures between 10-125 MPa. Petrographic thin sections and minicores for microtomography were prepared from the experimentally fractured samples. High-resolution three-dimensional (3D) microstructural data were then acquired using synchrotron-based X-ray microtomography at the Advanced Photon Source (APS), providing detailed visualization of fracture networks within the amphibolite rock matrix. Using the 3D image-analysis software Avizo, I will quantify key transport properties, including permeability and electrical conductivity, and relate them to the porosity of the rock fabric.

The permeability-porosity and electrical conductivity-porosity relationships are described using the Kozeny-Carman equation and Archie's Law, respectively. Using a digital rock physics approach, I perform numerical simulations of fluid flow and electrical current to determine the permeability and electrical conductivity of the fracture networks, enabling a direct comparison between their geometric characteristics and transport behavior. Fracture complexity is organized into three categories based on the number of fracture planes: simple, intersecting, and complex.

The power-law exponents for permeability and electrical conductivity of different fracture types are obtained from the numerical experiments. By linking fracture complexity and transport properties, this work will improve our understanding of rock deformation processes and inform models of fluid flow in fractured geothermal reservoirs.

Plain-Language Abstract

Investigation of the rock type, amphibolite, and its response to artificial fracturing provides further information for Enhanced Geothermal Systems (EGS) technology. In geothermal energy acquisition, energy in the form of heat is collected from beneath the Earth's surface. Harvesting renewable, thermal energy involves pumping water into the artificial fractures and recollecting the heated water at the surface of the crust in the form of steam. The goal of this project is to determine the power law relationship between porosity and permeability and porosity and conductivity for three fracture types in amphibolite. Four rock cores were sourced from testing wells in the Sanford Underground Research Facility (SURF) in Lead, South Dakota. This site provides access to crystalline rock where conductivity is measurable in EGS focused experiments. This project is important because the results provide permeability values, which are unattainable in situ at the SURF. The samples are fractured using a triaxial rock deformation press at room temperature and under pressure conditions that resemble the environment of the underground site where they were collected. Analysis of the fracture geometry as it relates to permeability-porosity and conductivity-porosity power law is conducted with the use of a 3D modelling software. In preparation for data analysis, the fractured rock cores are scanned with the use of X-ray microtomography. The data are then reconstructed into readable files for the 3D image datasets where quantitative information is extracted related to the permeability, conductivity, and porosity of the fractured amphibolite.

Table of Contents

Introduction and Background **5**

Figure 1: Underground Map of SURF 4100 Level 6

Method of Analysis **7**

Mechanical Fracturing of Amphibolite Cores *7*
Table 1: Mechanical Fracturing Pressure Conditions of Amphibolite Cores 8

Tomographic Data Collection *8*
Figure 2: Core Preparation for X-ray Microtomography 9

Rock Physics Approach *9*
Figure 3: Fracture Data Processing 10
Figure 4: Yates Amphibolite Photomicrographs 13

Fracture Geometry *14*
Figure 5: Fracture Geometry Types 14

Results **15**

Figure 6: DML1 and T-Series Simple Fractures: k vs φ 15
Figure 7: DML1 Intersecting Fractures: k vs φ 15
Figure 8: DML1 and T-Series Complex Fractures: k vs φ 16
Figure 9: DML1 and T-Series Simple Fractures: e vs φ 16
Figure 10: DML1 Intersecting Fractures: e vs φ 17
Figure 11: DML1 and T-Series Complex Fractures: e vs φ 17
Figure 12: DML1 and T-Series Simple Fractures: k vs e 18
Figure 13: DML1 Intersecting Fractures: k vs e 18
Figure 14: DML1 and T-Series Complex Fractures: k vs e 19
Figure 15: DML5 Complex Fractures: k vs φ 19
Figure 16: DML5 Complex Fractures: e vs φ 20
Figure 17: DML5 Complex Fractures: k vs e 20
Table 2: Permeability Exponent (n) for DML1 and T-Series Cores 21
Table 3: Conductivity Exponent (m) for DML1 and T-Series Cores 21
Table 4: Permeability-Conductivity Exponent 22
Table 5: DML5 Transport Property Relationships 22

Discussion **23**

Conclusions and Broader Implications **24**

Acknowledgements **25**

Bibliography **25**

Introduction and Background

Enhanced Geothermal Systems (EGS) hold potential in fulfilling energy gaps that arise with mass implementation of artificial intelligence, a booming internet presence in global communities, and an increasing world population. Traditional geothermal energy acquisition relies on the presence of natural reservoirs, while EGS is not geographically limited. In EGS, fractures are induced in the subsurface, after which water is pumped into an injection well and circulated through these engineered pathways. As the water reaches greater depths, it is heated and subsequently pumped to a production well. Electricity is generated when the steam exits the pressurized geothermal reservoir and powers turbines that are located above ground (Olasolo et al., 2016). Efficient fluid transmissivity in EGS relies heavily on controlled fracture induction.

Ideal fracture geometry and aperture, both of which remain under active investigation, reflect the complexity of fracture propagation. In a recent study exploring fracture analysis methods, the results describe the relationship between production and the angles of natural fracture paths with regard to overburden stress values (Sherratt et al., 2020). The results of this project conclude that fracture propagation is greatly influenced by the attributes of fracture angles, pre-existing fractures, and in situ stress conditions. Other important conditions that determine the path of the fracture include stress magnitude from tectonic forces, lithological composition, and pore fluid pressure. There are preferential streamlines through which water flows in. With an increase in aperture, the favored path condenses into the largest fracture channel, rather than smaller pathways (Guo et al., 2016). If aperture of the fracture is too large, fluid circulates too rapidly for productive heat transfer. Conversely, if the aperture too small, fluid permeability through the reservoir is significantly reduced. The efficiency of EGS declines in both instances (Lei et al., 2023). Thermal energy transfer occurs where the surface of the flowing fluid comes into contact with the rock matrix and energy acquisition relies on the heated fluid reaching the production well. Therefore, favorable conditions include widespread fracture networks that have the capacity to pump fluid proficiently (Guo et al., 2016). Mechanical effects from the fluid moving through the rock matrix lead to chemical dissolution and porelastic creep. Consequently, the alteration of fracture geometry depends on the rock type and array of mineral components (Ghassemi et al., 2008).

This project focuses on four borehole samples collected from the Sanford Underground Research Facility (SURF), each deformed with varying pressure conditions. The four core samples, DML1, DML5, TH41004 and TS4, are sourced from testing wells in the Lower unit (Yates Unit, informal) of the Poorman Formation in Lead, South Dakota (Figure 1). The SURF is an important laboratory that was developed from the remains of the Homestake Gold Mine and now serves as a base for scientific research across various disciplines (Fiorucci et al., 2013). Several geophysical studies are employed through the EGS Collab project at the SURF and they contribute to the objective of understanding hydraulic fracture patterns with regard to stress perturbations (Kneafsey et al. 2025; Johnson et al., 2024; Schwering et al., 2020). In situ

experiments at the SURF are coupled with laboratory measurements to quantify the electrical conductivity-porosity and permeability-porosity relationships.

For porous rocks, theoretical and experimental studies show a power-law relationship between permeability and porosity, i.e., the Kozeny-Carman equation (Carman, 1956).

$$k \propto \phi^n \tag{1}$$

where k is permeability, ϕ is porosity, and n is the power-law exponent. It is shown that the exponent n depends on pore geometry and connectivity. For a well-connected uniform pore network, n=2. For well-connected uniform fracture network, n=3 (e.g., David et al., 1994).

The electrical conductivity-porosity relationship can also be described using a power law, i.e., Archie's law (Archie, 1942).

$$F \propto \phi^m \tag{2}$$

where F is the electrical formation factor and m is the power-law exponent. The exponent m depends on pore geometry and connectivity. Formation factor links porosity with electrical conductivity, as there is more electrical potential in pore-space joints than in open pore-space (Revil & Cathles, 1999). The formation factor equation relates porosity to conductivity (Revil & Glover, 1997)

$$F = \frac{R}{R_f} \tag{3}$$

where F is a ratio of the electrical resistivity (R) to the resistivity of the fluid (R_f). Formation factor is scale invariant, and conductivity is inversely related to resistivity.

Figure 1: Underground Map of SURF 4100 Level

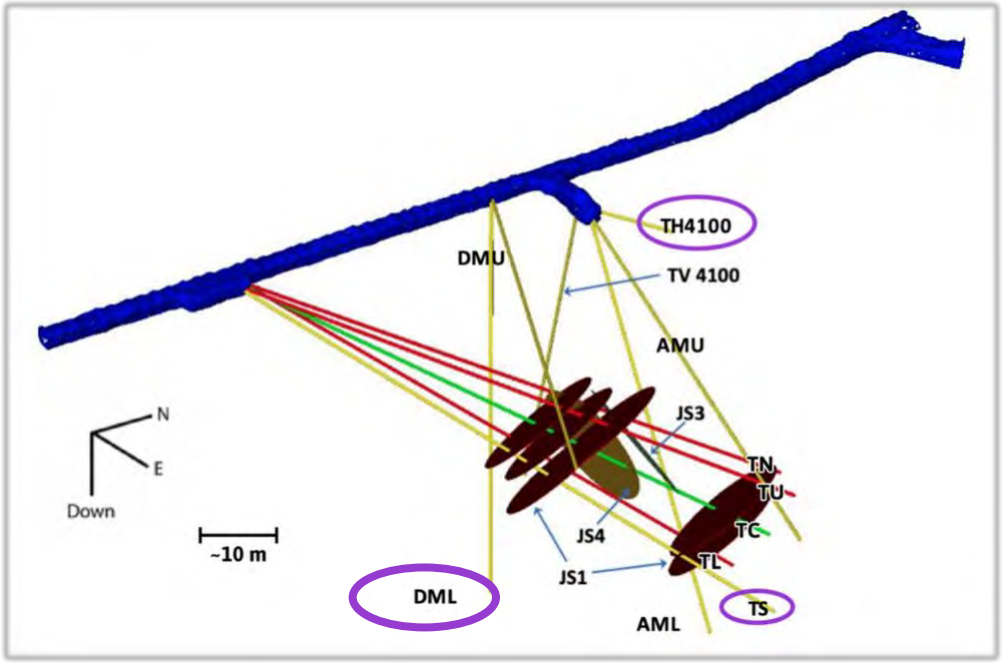


Figure 1. Borehole map of the 4100 level drift at the SURF (figure modified from Kneafsey et al. 2025). The blue line represents the mine tunnel at a depth of ~1.25 km. The yellow, red, and green lines represent monitoring, production, and injection wells respectively. The brown disks align with the natural fracture orientations. The four samples of interest for this project were collected from the DML, TH4100, and TS monitoring boreholes (circled in purple).

The major phases in the Yates amphibolite include ferro-magnesio-hornblende, oligoclase-andesine, calcite, dolomite, and ankerite. Accessory minerals include ilmenite, magnetite, titanite, pyrrhotite, and pyrite (Caddey et al., 1991). The sampled wells lie at a depth of ~1.25 km, where lithostatic pressure conditions exceed 30 MPa based on the density of crustal rock. In comparison to schist and rhyolite from the SURF, amphibolite demonstrated the greatest fracture toughness in an experiment analyzing fracture geometry in relation to mechanical properties of amphibolite (Jahnke et al., 2022). In my exploration of fracture geometry and the relationship between porosity of transport properties, four cores are mechanically fractured, and three-dimensional fracture network images are produced in the software program, Avizo, to collect permeability, conductivity, and porosity data.

Hypothesis:

The permeability exponent (n) and conductivity exponent (m), in relation to porosity, will change based on the fracture geometry type.

Null Hypothesis:

Fracture geometry is not an influential factor for the permeability exponent (n) nor the conductivity exponent (m) to differ in relation to porosity.

Method of Analysis

Mechanical Fracturing of Amphibolite Cores

The amphibolite cores were mechanically fractured in an Auto Lab 1500 New England Research (NER) apparatus located in the Rock Deformation Lab at the University of Maryland (UMD). TH41004 and TS4 core samples sustained deformation with confining pressure (Pc) of 35 MPa and pore fluid pressure (Pf) of 10 MPa. DML1 and DML5 core samples were deformed with confining pressures 35 and 150 MPa and pore fluid pressures 10 and 125 MPa, as outlined in Table 1. The cores were wrapped in metal jackets to maintain a confined environment similar to the rocks beneath the subsurface at SURF.

Table 1: Mechanical Fracturing Pressure Conditions of Amphibolite Cores

	DML 1	DML5	TS4	TH41004
Confining Pressure (P_c)	35 MPa	150 MPa	35 MPa	35 MPa
Pore Fluid Pressure (P_f)	10 MPa	125 MPa	10 MPa	10 MPa

Tomographic Data Collection

Following deformation, tomographic data of the deformed samples were collected at the Advanced Photon Source synchrotron using synchrotron-based X-ray microtomography. As the X-ray passes through the rock sample, different phases, i.e., minerals and fractures, absorb the photons to various degrees depending on density and composition. The sample, mounted on a rotational stage, is rotated from 0° to 180° during imaging. One thousand eight hundred 2D X-ray projection images (radiographs) were recorded at small angular increments of 0.1°. Each projection captures how internal features attenuate X-rays along a specific path through the sample. Due to the requirement of high-resolution data and the range of the X-ray beam, the cores were scanned in small subsections. First, the cylindrical cores were bisected along the longitudinal plane (Figure 2). Then, one side of each sample was divided along the transverse plane into ten slices, each slice containing five scanned sections labeled A-E. The other sides of the cylindrical cores were sliced longitudinally in preparation for thin sections.

At the UMD Geodynamics Laboratory, I digitally prepared the tomographic data for analysis with the rock physics approach. Data processing includes the reconstruction of files through the software program, IDL Tomo Display, so the files are compatible with Avizo, a 3D imaging software.

Figure 2: Core Preparation for X-ray Microtomography

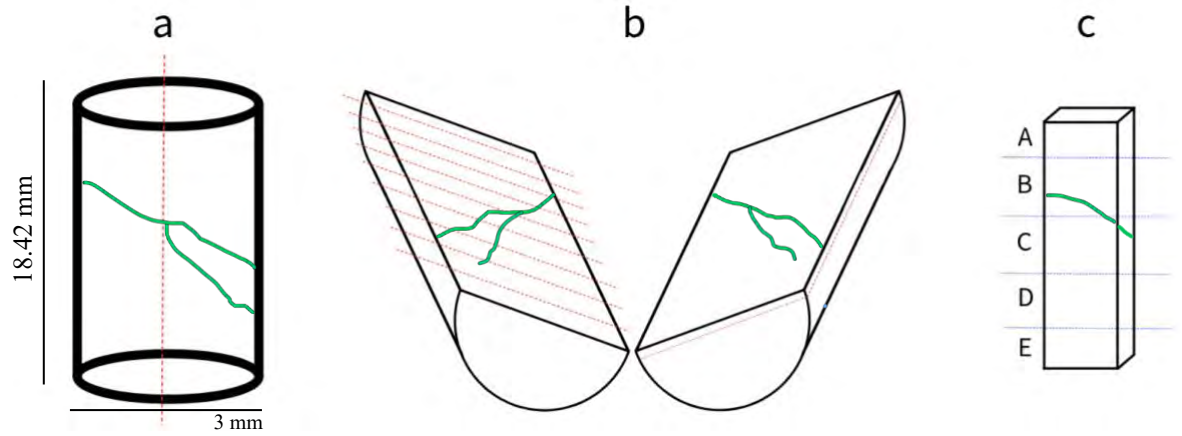
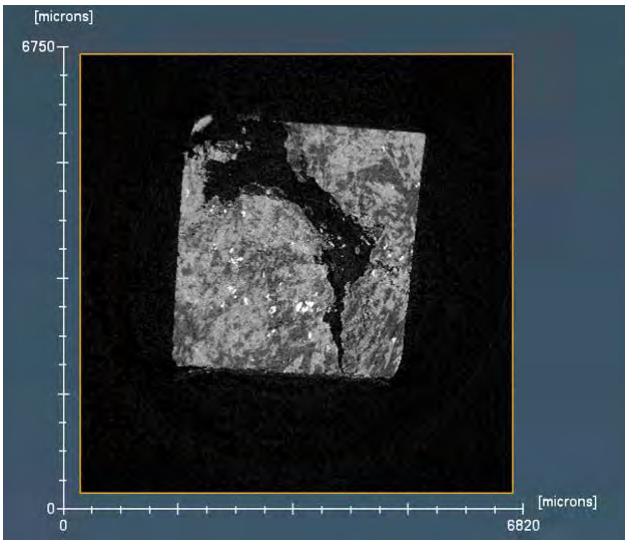


Figure 2. X-ray microtomography scan arrangement. (a) The cylindrical core was bisected along the longitudinal axis into two halves. (b) One half of the core was sliced transversely into ten subsections. The other half was sliced longitudinally, so a thin section was created from the face of the cylinder. (c) Each of the ten slices from the left half of the cylinder were cut into rectangular prisms and scanned five sections labeled A-E. Red lines indicate slices, blue lines indicate scan boundaries, and green lines represent fractures.

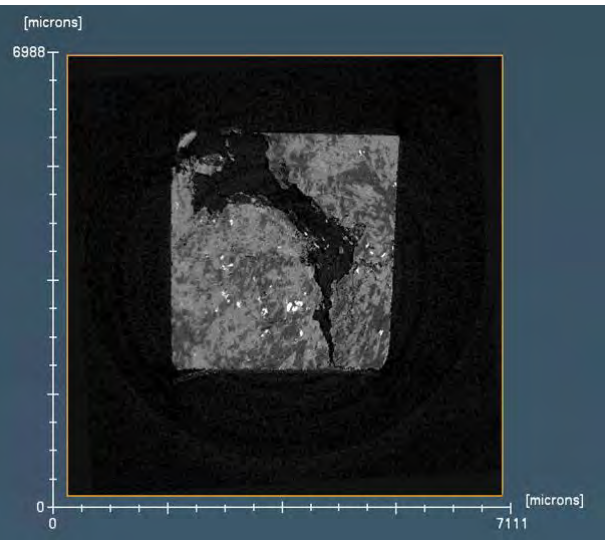
Rock Physics Approach

The rock physics approach involved loading 2048 reconstructed tomography .tiff data files for each slice into the 3D imaging software, Avizo. Once the files were loaded into the program (Figure 3a), the images were transformed and resampled in order to preserve data during the cropping process (Figure 3b). A subvolume was extracted to isolate the rock matrix from the blank background (Figure 3c). Smoothing and noise-reduction techniques were employed through the use of the median filter tool (Figure 3d). The fracture network was then thresholded from the matrix of the rock fabric by separating the two opposing phases based on contrasting colors (Figure 3e). Volume rendering is a tool employed in Figure 3f which segments the fracture network from the rock matrix. The fracture appears as the darkest phase, while the rock matrix includes a range of greyscale components. The heavier minerals in the sample absorb more X-rays and therefore show up as lighter colored material. Based on the known mineral composition of amphibolite, my estimation is that the bright white minerals in lower abundance are denser minerals such as magnetite and titanite. Light grey represents ferro-magnesio-hornblende and the dark grey represents lighter minerals such as calcite, dolomite, and ankerite.

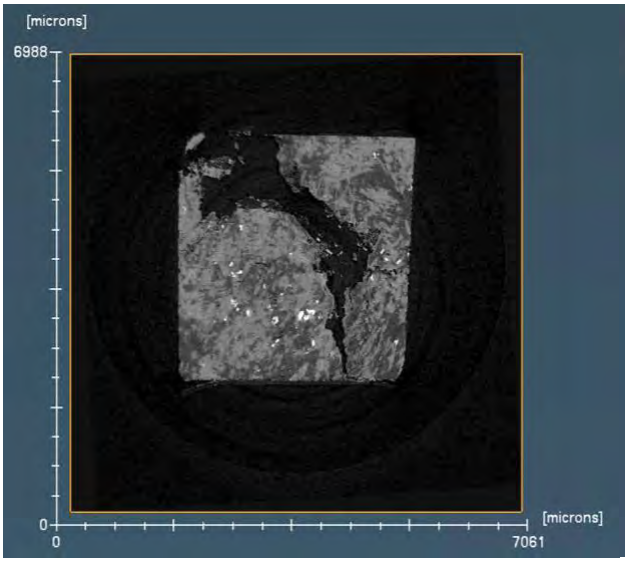
Figure 3: Fracture Data Processing



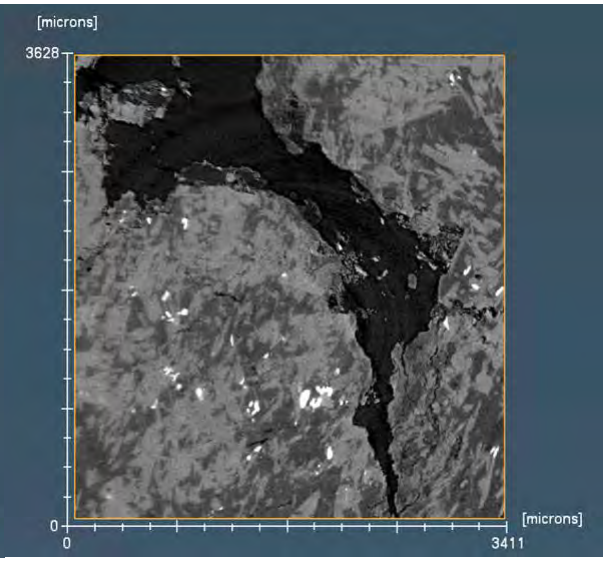
3a. Original image (slice 670)



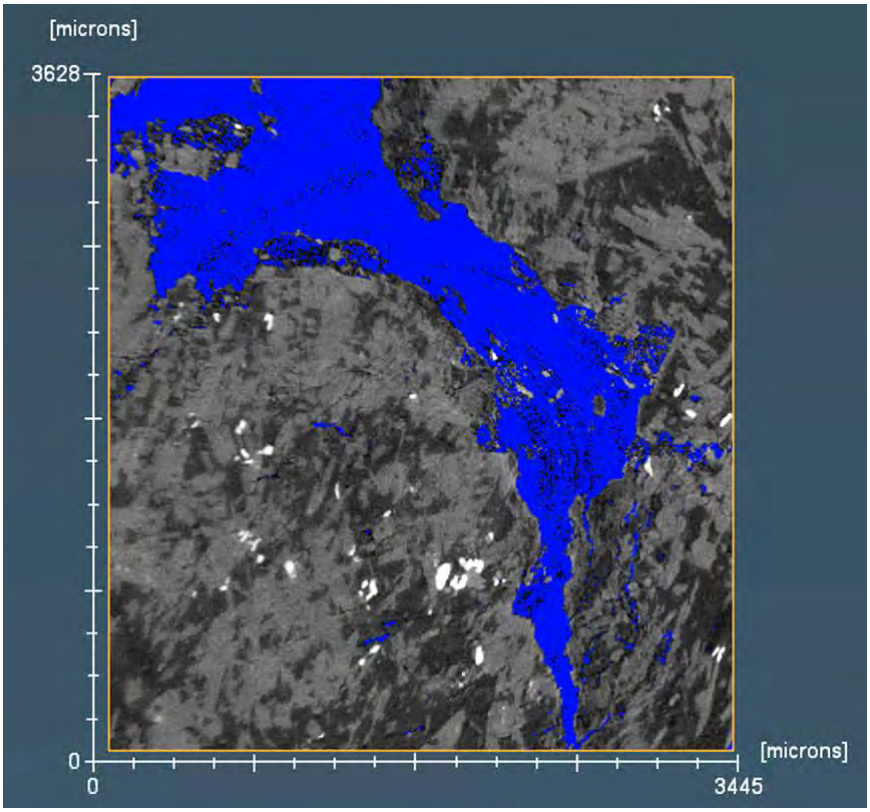
3b. Transformed image



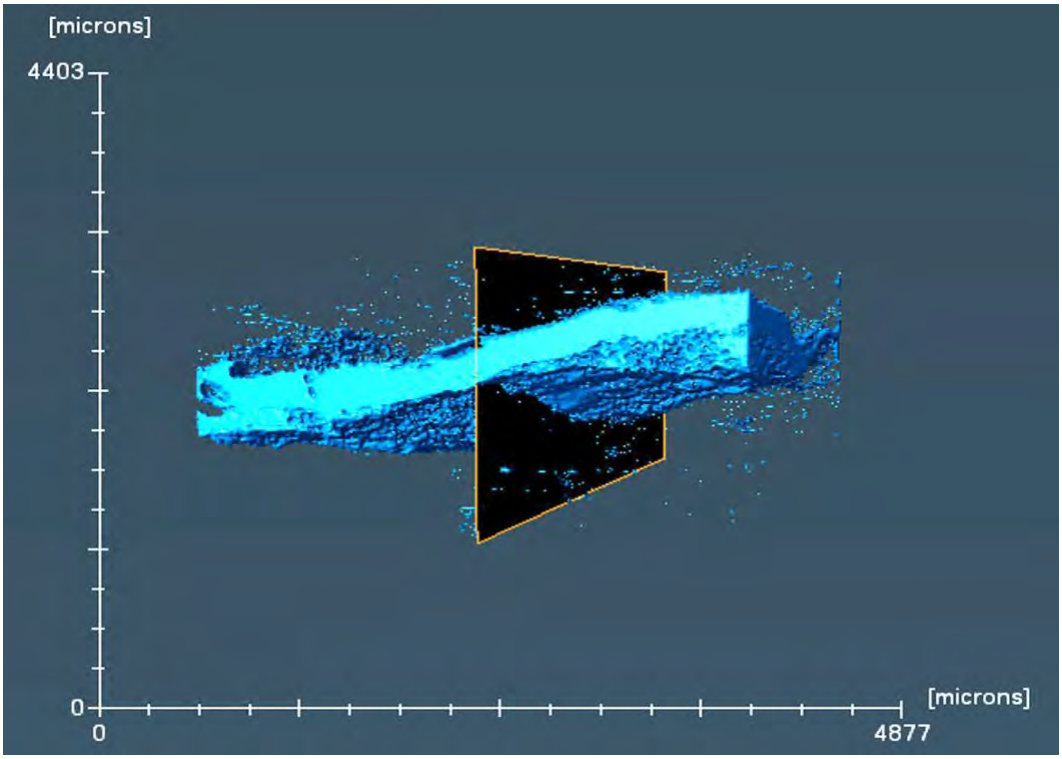
3c. Median filtered image



3d. Subvolume extracted



3e. Thresholded image



3f. Volume rendering: three-dimensional profile

Figure 3. Data processing of section 6C, slice 670 in three-dimensional (3D) imaging software (Avizo). (a) The reconstructed and unedited tomographic data were loaded into Avizo and (b) the transformed and resampled image was aligned to the axes of the sample to those of the viewing window shown in orange. (c) A filter is applied to the realigned image and (d) the border is cropped to account for only the rock matrix. (e) The fracture plane is captured in blue and separated from the rock matrix with the use of the thresholding tool. (f) With use of the volume rendering tool, the fracture plane is constructed into a 3D profile and tilted at an angle to showcase the 3D space.

Once the fracture network was isolated and modeled in a three-dimensional field, permeability data were collected through the use of a Darcy's Law based simulation (Darcy, 1856).

$$\frac{Q}{S} = -\frac{k}{\mu}\frac{P_{in}-P_{out}}{L} \quad (4)$$

Q represents Darcy velocity, S is the cross-sectional area, k is permeability, μ is viscosity, P is pressure, and L is the subvolume length. Conductivity is also acquired with the absolute permeability simulation. Porosity data is collected through the use of the volume fraction tool. Subvolume sizes were kept consistent at 550 by 550 by 550 voxel cubes (~1251 μm by ~1251 μm by ~1251 μm).

Permeability differs from conductivity due to the inability to properly estimate its value in situ. Permeability is derived through the application of Darcy's Law in relation to the vector-based Navier-Stokes equation, whereas conductivity is determined using the scalar Laplace equation (Sahimi, 1993). Simulations in Avizo serve as a tool for the visualization and analysis of fracture properties, including permeability. Data extracted from this program fills permeability data gaps for in situ EGS experiments at the SURF.

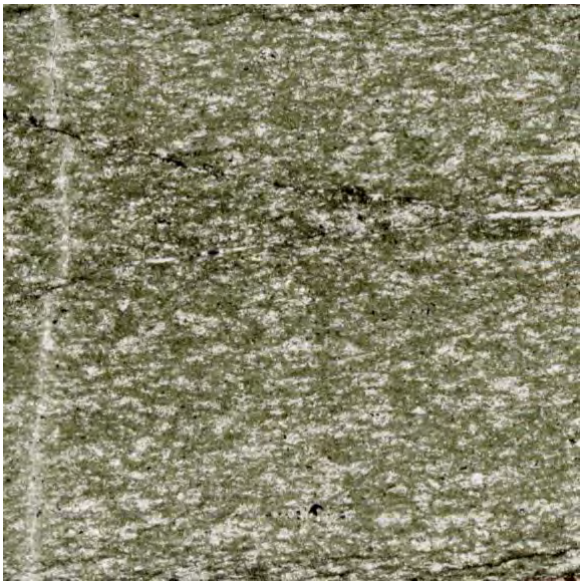
Figure 4: Yates Amphibolite Photomicrographs



DML 1



DML 5



TS4



TH41004

Figure 4. dimensions of the photomicrographs are 18.4 mm by 18.4 mm. The fractures appear white in DML1, DML5, and TH41004. The fracture in TS4 has a black outline and interacts with a white calcite vein.

Fracture Geometry

After 3D mapping several fractures, we recognized a pattern in their morphology. We organized them into three categories: simple, intersecting, and complex (Figure 5). Simple is a planar feature representing fractures that only have one main chamber. Intersecting involves two fracture planes that interact with one another or a plane that divergences into two pathways. Complex accounts for the fractures that have more than two planar features that interact. Permeability-porosity and conductivity-porosity relationships are plotted based on the fracture type to evaluate if the exponent differs with complexity.

Figure 5: Fracture Geometry Types

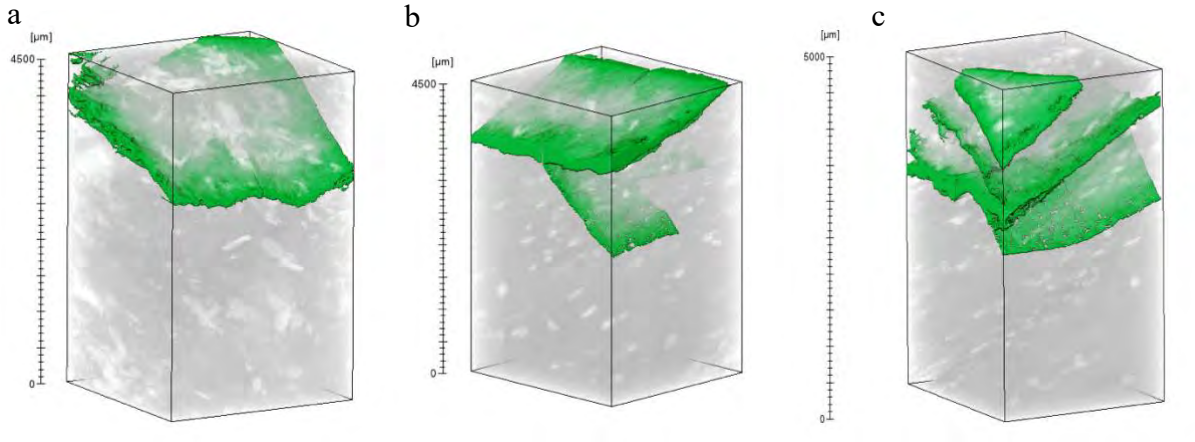


Figure 5. Three-dimensional fracture network depicted in the rock matrix. The matrix has decreased opacity to showcase the fracture structure. (a) simple, (b) intersecting, and (c) complex.

Results

Permeability-Porosity Plots

Figure 6: DML1 and T-Series Simple Fractures: k vs φ

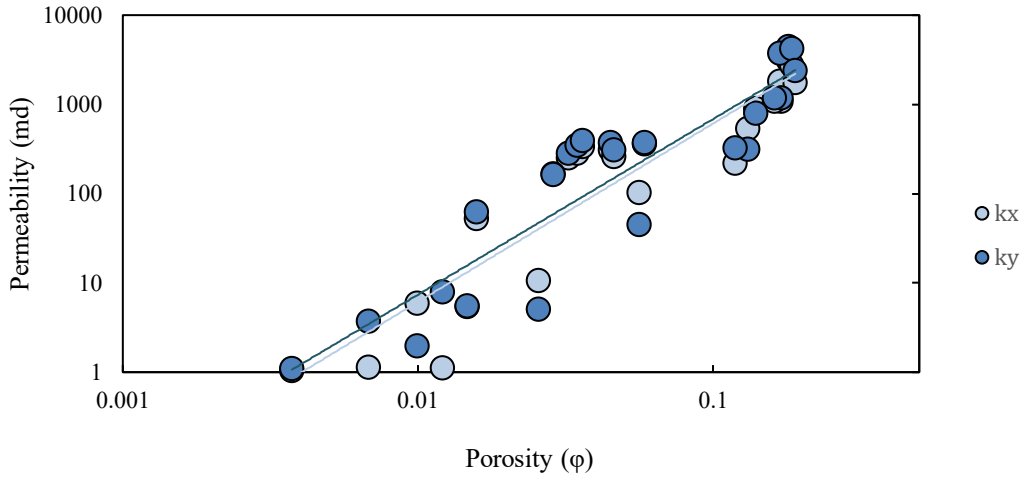


Figure 6. DML1, TS4, and TH41004 were combined onto one plot because they sustained deformation at a P_f of 10MPa. The exponent was derived from the slope of the light blue trendline (kx) and the dark blue trendline (ky). n= 2.00$\pm$0.18 for kx and n=1.97$\pm$0.19 for ky.

Figure 7: DML1 Intersecting Fractures: k vs φ

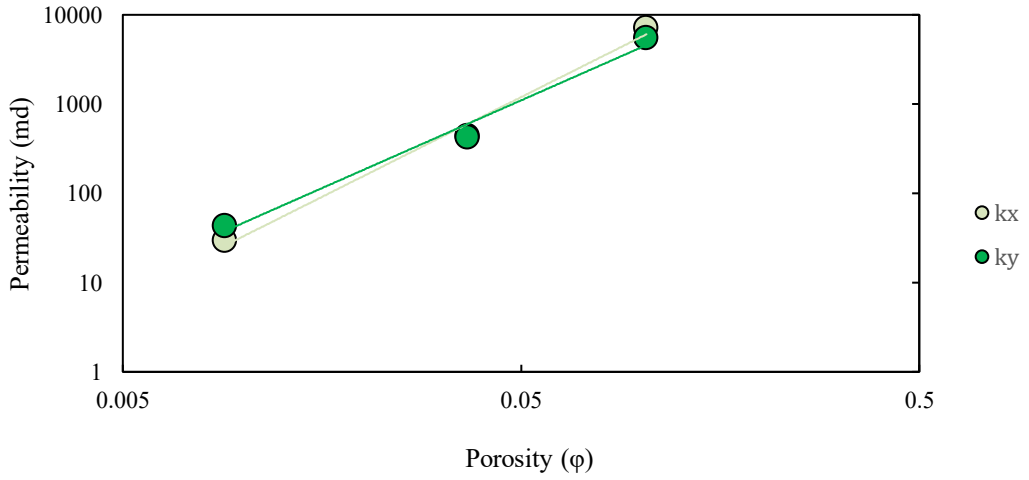


Figure 7. Intersecting fractures were plotted for only the DML1 borehole due to a lack of representative fracture geometry from the T-series boreholes. n=2.24$\pm$0.21 for kx and n= 1.97$\pm$0.24 for ky.

Figure 8: DML1 and T-Series Complex Fractures: k vs φ

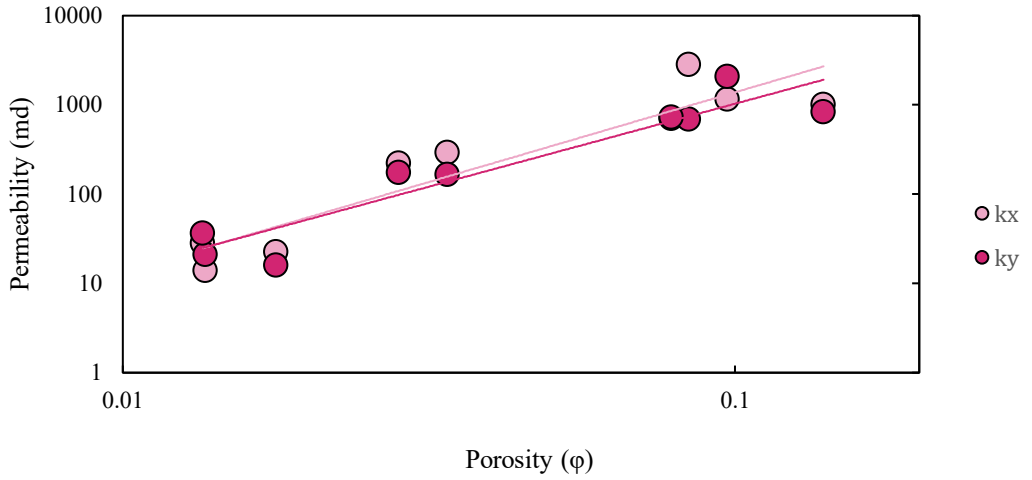


Figure 8. n =2.01±0.29 *for kx and n= 1.86*±0.25 *for ky.*

Conductivity-Porosity Plots

Figure 9: DML1 and T-Series Simple Fractures: e vs φ

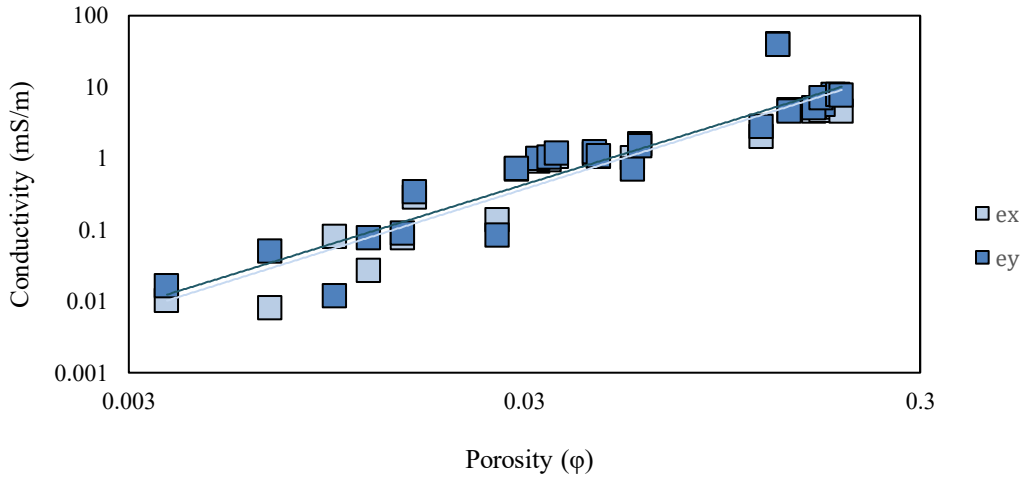


Figure 9. Squares represent conductivity-porosity relationships. m=1.73±0.14 *for ex and m=1.71*±0.14 *for ey.*

Figure 10: DML1 Intersecting Fractures: e vs φ

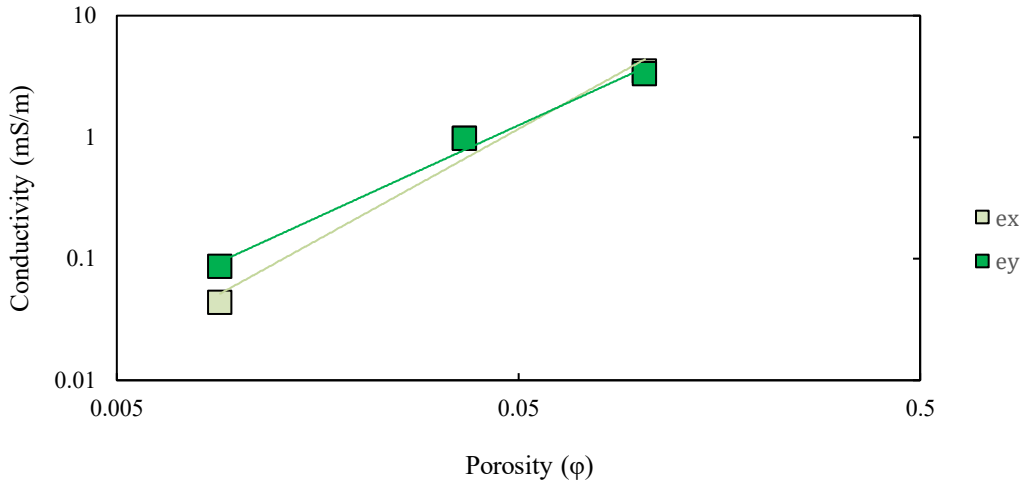


Figure 10. Intersecting fractures were plotted for only the DML1 borehole due to a lack of representative fracture geometry from the T-series boreholes. m=1.88±0.13 for ex and m= 1.65±0.12 for ey.

Figure 11: DML1 and T-Series Complex Fractures: e vs φ

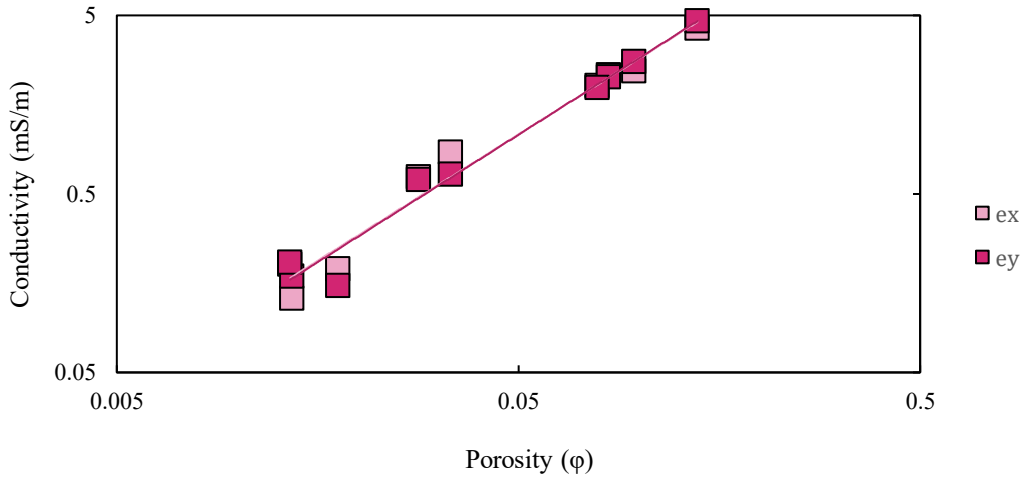


Figure 11. m=1.41±0.09 for ex and 1.43±0.09 for ey.

Permeability-Conductivity Plots

Figure 12: DML1 and T-Series Simple Fractures: k vs e

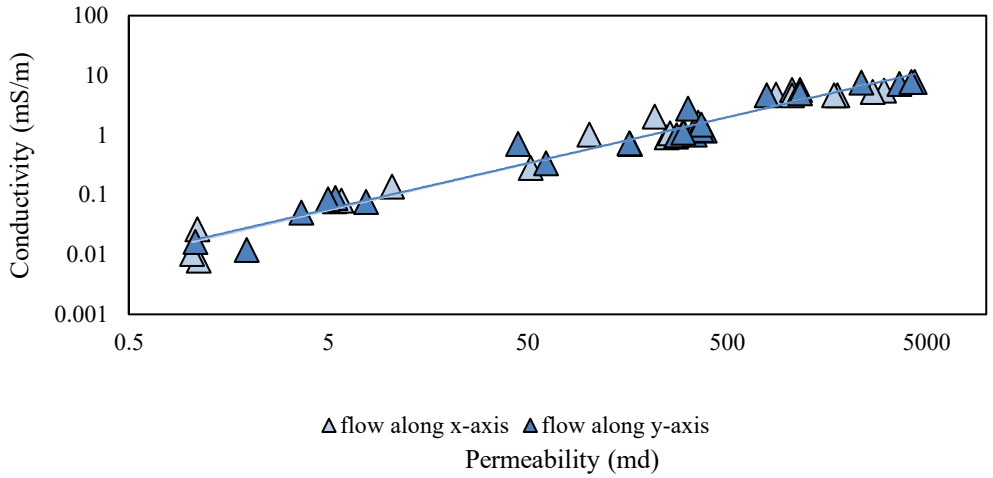


Figure 12. Triangles represent permeability-conductivity relationships. The exponent values for simple fractures are $0.78 \pm 2.5 * 10^{-4}$ *for the x-axis flow direction and* $0.77 \pm 1.9 * 10^{-4}$ *for the y-axis flow.*

Figure 13: DML1 Intersecting Fractures: k vs e

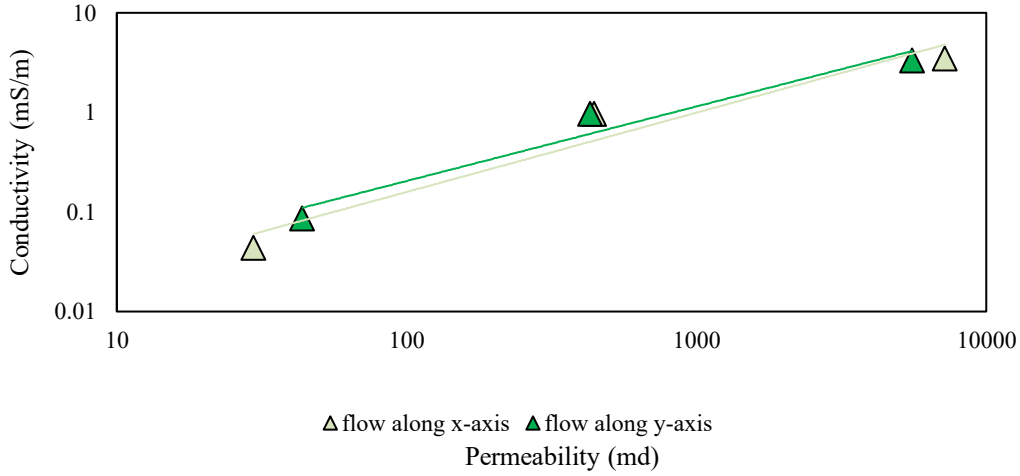


Figure 13. The exponent values for intersecting fractures are $0.80 \pm 9.4 * 10^{-5}$ *for the x-axis flow direction and* $0.75 \pm 1.1 * 10^{-4}$ *for the y-axis flow.*

Figure 14: DML1 and T-Series Complex Fractures: k vs e

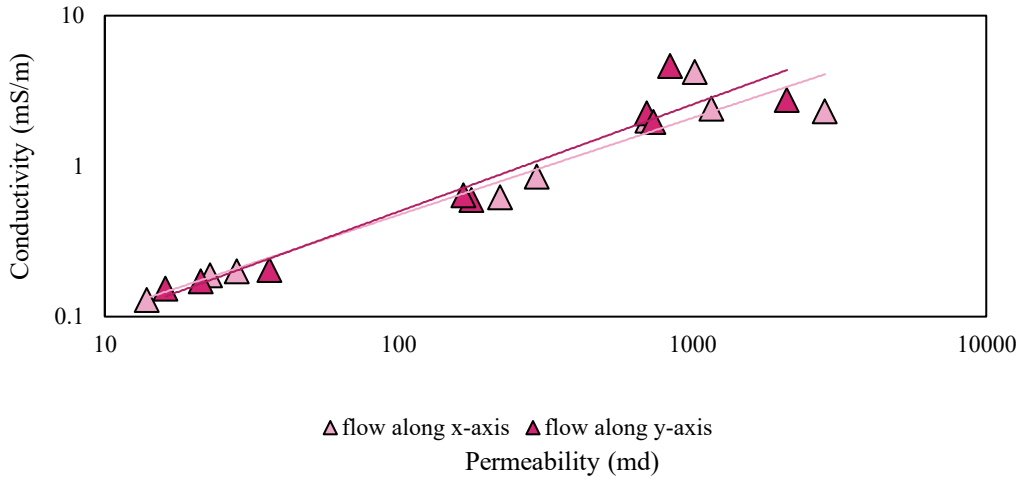


Figure 14. The exponent values for complex fractures are $0.64 \pm 6.2 * 10^{-4}$ *for the x-axis flow direction and* $0.71 \pm 2.8 * 10^{-5}$ *for the y-axis flow.*

DML5 Transport Property Plots

Figure 15: DML5 Complex Fractures: k vs φ

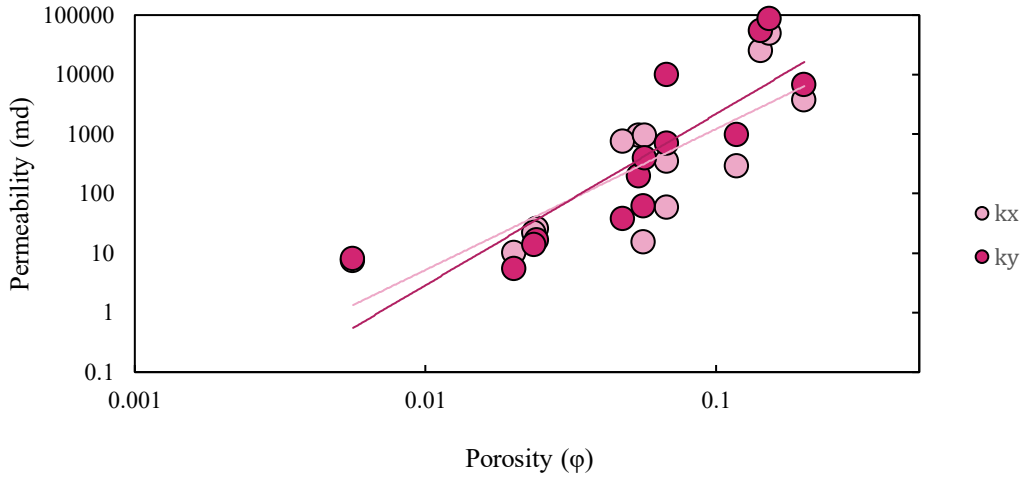


Figure 15. DML5 is plotted separately due to sustaining a higher pore fluid pressure of 125 MPa during deformation. $n = 2.37 \pm 0.52$ *for kx and* $n = 2.89 \pm 0.52$ *for ky.*

Figure 16: DML5 Complex Fractures: e vs φ

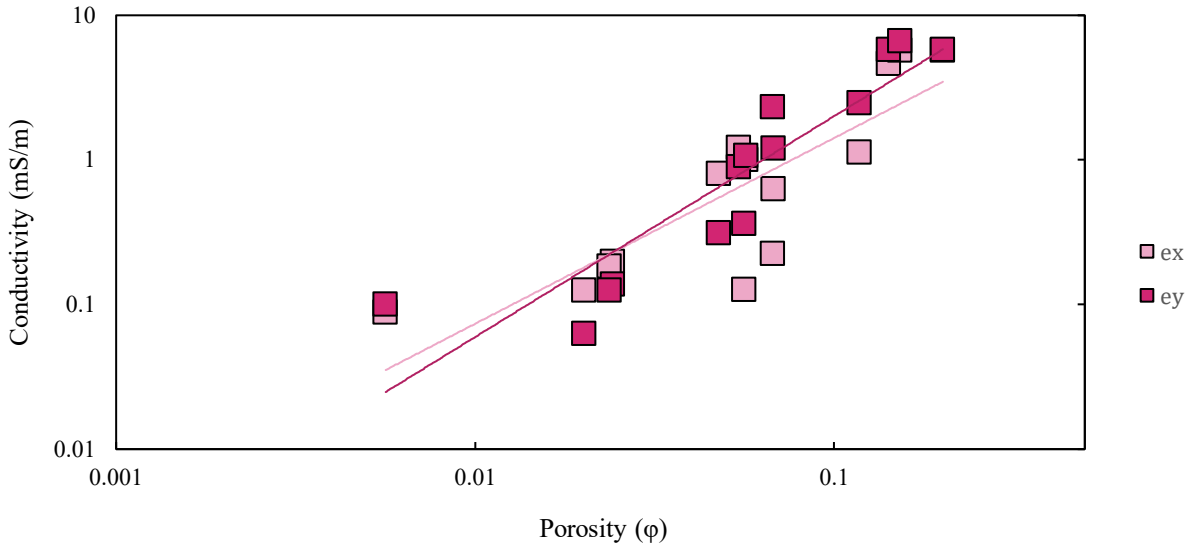


Figure 16. m = 1.28 ± 0.24 *for ex and m =1.53*± 0.21 *for ey.*

Figure 17: DML5 Complex Fractures: k vs e

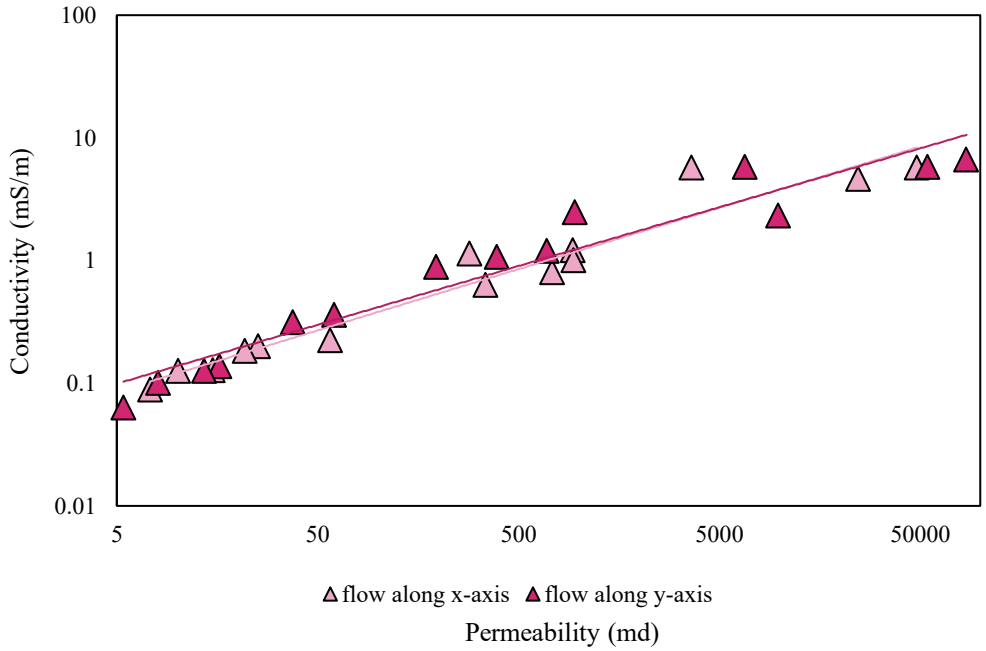


Figure 17. The exponent values for simple fractures are $0.50 \pm 2.8 * 10^{-5}$ *for the x-axis flow direction and* $0.48 \pm 1.6 * 10^{-5}$ *for the y-axis flow.*

Table 2: Permeability Exponent (n) for DML1 and T-Series Cores

	Simple		Intersecting		Complex	
Flow axis	*kx*	*ky*	*kx*	*ky*	*kx*	*ky*
Exponent	2.00±0.18	1.97±0.19	2.24±0.21	1.97±0.24	2.01±0.29	1.86±0.25
R^2	0.80	0.71	0.99	0.99	0.27	0.42

Table 3: Conductivity Exponent (m) for DML1 and T-Series Cores

	Simple		Intersecting		Complex	
Flow axis	*ex*	*ey*	*ex*	*ey*	*ex*	*ey*
Exponent	1.73±0.14	1.71±0.14	1.88±0.13	1.65±0.12	1.41±0.09	1.43±0.09
R^2	0.13	0.21	0.94	0.89	0.99	0.99

Table 4: Permeability-Conductivity Exponent

	Simple		Intersecting		Complex	
Flow axis	*x*	*y*	*x*	*y*	*x*	*y*
Exponent	0.78 $\pm 2.5 * 10^{-4}$	0.77 $\pm 1.9 * 10^{-4}$	0.80 $\pm 9.4 * 10^{-5}$	0.75 $\pm 1.1 * 10^{-4}$	0.64 $\pm 6.2 * 10^{-4}$	0.71 $\pm 2.8 * 10^{-5}$
R^2	0.83	0.89	0.97	0.98	0.55	0.59

Table 5: DML5 Transport Property Relationships

	k - φ		e - φ		k - e	
Flow axis	*kx*	*ky*	*ex*	*ey*	*x*	*y*
Exponent	2.37±0.52	2.89±0.52	1.28 ± 0.24	1.53±0.21	0.50 $\pm 2.8 * 10^{-5}$	0.48 $\pm 1.6 * 10^{-5}$
R^2	0.23	0.19	0.85	0.86	0.74	0.81

Uncertainty calculation

Uncertainty of the power law exponent, represented by the slope of the line of best fit, was calculated with the residual variance formula

$$S^2 = \frac{\sum(y_i - \hat{y}_i)^2}{n-2} \quad (5)$$

where S is residual variance, y_i is the log of permeability or conductivity, $\hat{y}_i$ is the predicted value based on the line of best fit, and n is the number of data points. The difference between y_i and $\hat{y}_i$ describes how far each data point lies from the line of best fit.

Once the residual variance is calculated, it is plugged into

$$SE(n) = \sqrt{\frac{S^2}{\sum_{i=1}^{n}(x_i - \bar{x}_i)^2}} \quad (6)$$

where SE is the standard error of the slope, x_i is the log of porosity, and $\bar{x}_i$ is the mean of porosity.

Discussion

The purpose of this research was to constrain exponent values for the power law relationships for permeability-porosity and conductivity-porosity. Fractures with simple, intersecting, and complex geometry were plotted with porosity versus permeability and conductivity to obtain power law relationship exponents. Permeability and conductivity data was collected in the x and y flow directions to account for anisotropy. Simple fracture geometry for permeability versus porosity exhibited the lowest exponent value for n at 2.00 ± 0.18 in the x flow direction and 1.97 ± 0.19 for the y-direction. Complex had a slightly higher kx value, 2.01 ± 0.29, but the lowest ky value of the three fracture geometries, 1.86 ± 0.25. Intersecting had the highest kx for the permeability-porosity relationship with an exponent value of 2.24 ± 0.21, but the same ky exponent as the simple fractures, 1.97 ± 0.19. Intersecting exponent, n, was closest to the expected value for the permeability-porosity power law relationship, n=3 (David et al., 1994). Possible reasons for a lower n value include the extent of fracture roughness and the intricacy of the pore network. Even though the simple fractures appear to be one single plane, they undulate and therefore may contain irregular fluid pathways that affect the permeability.

Conductivity-porosity relationships showed a wider range of values for exponent m, with complex fracture geometry at the lowest kx and ky, 1.41 ± 0.09 and 1.43 ± 0.09. Intersecting fractures had more anisotropy with a greater difference between the kx and ky values, 1.88 ± 0.13 and 1.65 ± 0.12. Intersecting fractures were plotted for only the DML1 borehole due to a lack of representative fracture geometry from the T-series boreholes. Simple fractures had kx and ky values of 1.73 ± 0.14 and 1.71 ± 0.14 respectively for exponent m. All of the fracture geometries

fell in close range to the theoretical value of m, calculated with the assumption of spherical grains by an effective-medium theory (EMT). Sen et al. (1981) derived this relationship with EMT, considering a theoretical spherical grain coated by a material of similarly coated grains. The calculated value for m was 1.5 and the complex fracture type matched this estimate with consideration of the uncertainty. In the same study, Sen et al. predicted that the higher m values seen in the simple and intersecting fractures may be a result of a less spherical grain shape.

Permeability plotted with conductivity was an important visualization of the dataset because it showcased the connection between conductivity, which can be collected in situ, and permeability, which relies on lab collection. The power law relationship between the two allowed for the computation of permeability for in situ projects at SURF from conductivity data. Exponents for the relationship between permeability and conductivity range from $0.64 \pm 6.2 * 10^{-4}$ to $0.80 \pm 9.4 * 10^{-5}$. Unlike the permeability-porosity and conductivity-porosity relationships, this exponent does not represent a direct empirical constant. Electric conductivity behaves differently than permeability because electrical current branches across the rock matrix regardless of a fully connected grain network. Pore space morphology create complex systems for conductivity (Cai et al., 2017).

DML5 displayed a permeability-porosity exponent relationship in close proximity to the expected n value of 3. The kx had an n value of 2.37 ± 0.52 and the ky had $n=2.89 \pm 0.52$. The R^2 values for these exponents are lower (0.23 and 0.19 respectively) due to notable outliers in slice 5, part B. The electric conductively also matched the theoretical exponent value well for the DML dataset (ex=1.28 ± 0.24 and ey=1.53 ± 0.21). With the high pore fluid pressure conditions, this rock core sustained more damage, and the fractures networks were highly complex. There was a higher quantity of pathways for fluid to flow through in this fracture type. Overall, the m and n exponents contrast between the fracture types, but the only clear disposition is to support the hypothesis is the complex fracture type featuring a lower electrical conductivity exponent (m). The intersecting fracture type presents inconsistently, and this is likely due to a small sample size.

Conclusions and Broader Implications

Ultimately, through this project I aim to further our knowledge of how porosity relates to permeability and conductivity in a power law relationship. Transport properties are investigated in regard to fracture geometry. By analyzing these relationships on a microscopic scale, we can improve our ability to predict fracture behavior in enhanced geothermal systems. Future work includes analyzing additional borehole datasets to improve on the precision of the exponent value. Another consideration to build upon in furthering this research is investigating the subvolume size effect on the statistical results. For this study, it is essential to maintain consistency in the subvolume sample size to mitigate variation in the power law relationship as a result of scale. Comparison between multiple subvolume sizes will offer insight into the effect of scale change that occurs from the lab to in situ experiments.

Acknowledgements

This research was made possible by my thesis advisor, Dr. Wenlu Zhu. Her guidance throughout the past year inspired my endeavors to continue my professional track in a career related to geothermal energy. She exemplified patience and kindness when I asked for clarification on relevant knowledge gaps. With her support I felt intellectually challenged and highly motivated by my research topic.

Dr. Phil Piccoli invested time to direct me towards a research group that aligned with my future goals. He also fostered a sense of confidence I had yet to capture in my scientific endeavors. I greatly appreciate the opportunities he presented to me to explore my academic potential.

Dr. Tommaso Mandolini and I worked closely on this project. His unwavering dedication to my success was reflected by the initiative he took to teach me how to use the 3D imaging software and countless hours of transport property discussion.

I also want to extend my gratitude to Dr. Travis Hager, Megan Ryan, Sourabh Shubham, and Dr. Laurent Montési for welcoming me into the geodynamics laboratory group.

Bibliography

Archie, G. E. (1942). The electrical resistivity log as an aid in determining some reservoir characteristics. *Journal of Petroleum Technology, 146*, 54–62. https://doi.org/10.2118/942054-G

Caddey, S. W., Bachman, R. L., Campbell, T. J., Reid, R. R., & Otto, R. P. (1991). The Homestake gold mine: An early Proterozoic iron-formation-hosted gold deposit, Lawrence County, South Dakota. *U.S. Geological Survey Bulletin, 1857-J*, J1–J67. https://doi.org/10.3133/b1857J

Cai, J., Wei, W., Hu, X., & Wood, D. A. (2017). Electrical conductivity models in saturated porous media: A review. *Earth-Science Reviews, 171*, 419–433. https://doi.org/10.1016/j.earscirev.2017.06.013

Carman, P. C. (1956). *Flow of gases through porous media*. Academic Press.

Darcy, H. (1856). *Les fontaines publiques de la ville de Dijon*. Victor Dalmont.

David, C., Wong, T.-f., Zhu, W., & Zhang, J. (1994). Laboratory measurement of compaction-induced permeability change in porous rock: Implications for the generation and maintenance of pore pressure excess in the crust. *Pure and Applied Geophysics, 143*, 425–456.

Fiorucci, S., Gilchriese, M. G., Lesko, K. T., & Sanford Underground Research Facility. (2013). The Sanford Underground Research Facility at Homestake. *Journal of Physics: Conference Series, 460*, 012018. https://doi.org/10.1088/1742-6596/460/1/012018

Ghassemi, A., Nygren, A., & Cheng, A. H.-D. (2008). Effects of heat extraction on fracture aperture: A poro–thermoelastic analysis. *Geothermics, 37*(5), 525–539. https://doi.org/10.1016/j.geothermics.2008.06.001

Guo, B., Fu, P., Hao, Y., Peters, C. A., & Carrigan, C. R. (2016). Thermal drawdown-induced flow channeling in a single fracture in EGS. *Geothermics, 61*, 46–62. https://doi.org/10.1016/j.geothermics.2016.01.004

Jahnke, B., Ruplinger, C., Bate, C. E., Trzeciak, M., Sone, H., & Wang, H. F. (2022). Fracture toughness of schist, amphibolite, and rhyolite from the Sanford Underground Research Facility (SURF), Lead, South Dakota. *Scientific Reports, 12*, 15941. https://doi.org/10.1038/s41598-022-20031-y

Johnson, T. C., Burghardt, J., Strickland, C., Sirota, D., Vermeul, V., Knox, H., Schwering, P., Blankenship, D., Kneafsey, T., & EGS Collab Team. (2024). 4D electrical resistivity imaging of stress perturbations induced during high-pressure shear stimulation tests. *Geophysical Research Letters, 51*. https://doi.org/10.1029/2024GL108423

Kneafsey, T., et al. (2025). The EGS Collab project: Outcomes and lessons learned from hydraulic fracture stimulations in crystalline rock at 1.25 and 1.5 km depth. *Geothermics, 126*, 103178. https://doi.org/10.1016/j.geothermics.2024.103178

Lei, Z., Zhang, Y., Cui, Q., et al. (2023). The injection-production performance of an enhanced geothermal system considering fracture network complexity and thermo-hydro-mechanical coupling in numerical simulations. *Scientific Reports, 13*, 14558. https://doi.org/10.1038/s41598-023-41745-7

Olasolo, P., Juárez, M. C., Morales, M. P., D'Amico, S., & Liarte, I. A. (2016). Enhanced geothermal systems (EGS): A review. *Renewable and Sustainable Energy Reviews, 56*, 133–144. https://doi.org/10.1016/j.rser.2015.11.031

Revil, A., & Cathles, L. M. (1999). Permeability of shaly sands. *Water Resources Research, 35*(3), 651–662. https://doi.org/10.1029/98WR02700

Revil, A., & Glover, P. W. J. (1997). Theory of ionic-surface electrical conduction in porous media. *Physical Review B, 55*(3), 1757–1773.

Sahimi, M. (1993). Flow phenomena in rocks: From continuum models to fractals, percolation, cellular automata, and simulated annealing. *Reviews of Modern Physics, 65*(4), 1393–1534. https://doi.org/10.1103/RevModPhys.65.1393

Schwering, P. C., Doe, T. W., Roggenthen, W. M., Neupane, G. H., Johnston, H., Dobson, P. F., Ulrich, C., Singh, A., Uzunlar, N., & Reimers, C. (2020). Deterministic discrete fracture network (DFN) model for the EGS Collab Project on the 4850 Level of the Sanford Underground Research Facility (SURF). *Proceedings of the 54th U.S. Rock Mechanics/Geomechanics Symposium*. American Rock Mechanics Association.

Sen, P. N., Scala, C., & Cohen, M. H. (1981). Self-similar model for sedimentary rocks with application to the dielectric constant of fused glass beads. *Geophysics, 46*(5), 781–795.

Sherratt, J., Haddad, A. S., Rafati, R., & Manzari, M. T. (2020). A fracture upscaling method (FUM) for hydraulically fractured reservoirs: From discrete fracture modelling to finite

difference simulations. *Journal of Natural Gas Science and Engineering, 83*, 103611. https://doi.org/10.1016/j.jngse.2020.103611

Honor Statement:

I pledge on my honor that I have not given or received any unauthorized assistance on this assignment/examination.